Supplementary Material

1 APPENDIX

1.1 Inversion Technique

To solve the inverted problem of extracting a differential energy flux from electron densities, we used the process outlined in Semeter and Kamalabadi (2005). We assumed the pitch angle distribution of the incoming electrons was isotropic and used the universal energy dissipation function (Λ) given in the paper. We took our range-energy function from Barrett and Hays (1976) as

$$R = 4.7 \times 10^{-6} + 5.36 \times 10^{-5} K^{1.67} - 0.38 \times 10^{-7} K^{-0.7} \qquad [\mathrm{kg \cdot m^{-2}}]$$

where K is the electron energy in keV. Using these, we can construct a matrix A, where

$$A_{ij} = \frac{\Lambda\left(\frac{s(z_i)}{R(K_j)}\right) \rho(z_i) K_j \Delta K_j}{35.5 R(K_j)}$$

where $s(z_i) = \sec(\theta) \int_{z_0}^{\infty} \rho(z)\, dz$ is the mass distance traveled by an electron as a function of altitude. We assumed the dip angle of the magnetic field, $\theta \approx 0$. We calculated the neutral atmospheric density $\rho(z)$ using the NRLMSISE00 model and approximated $z \to \infty$ as $z = 1000$ km (Hedin, 1991).

The matrix A relates the ion production rate (q) and the differential number flux (ϕ) via

$$q_i = A_{ij} \frac{\phi_j}{\Delta K_j}$$

As Fang et al. (2010) showed, using a range-energy function gives poor estimates of the ion production rate from electrons below 1 keV. However, the altitude range of the PFISR data means that there is very little, if any, contribution from these energies. Therefore, we assume that the range-energy function is a good enough estimate in this case.

Given that the inversion is done in terms of the ion production rate, we must convert our electron density into an ion production rate. Once we have done this we can compare the model to reality and perform the iterative process involved in the inversion. Important atmospheric chemistry is encapsulated in the conversion of electron density measured by PFISR to an ion production rate. This is especially relevant below 85 km, where the chemistry of ion production becomes increasingly complex (Mitra, 1981). There are several ways of handling the chemistry. For our primary results we used the Glukhov-Pasko-Ina (GPI) model (Glukhov et al., 1992; Lehtinen and Inan, 2007). This uses the specific conditions as measured by PFISR, and modeled by the International Reference Ionosphere (IRI-2016) and NRLMSISE-00. From this, it outputs an ion production rate as a function of altitude. This is what the algorithm compares to the modeled ion production rate.

Previous work has shown that GPI performs well for the D-region (Marshall et al., 2019). We set the values above 90 km to those of Gledhill (1986) for nighttime aurora. The Gledhill model is suitably close that of Vickrey et al. (1982) above 90 km and the Vickrey model performs well in this region (Sivadas et al., 2017). While we could have used the Vickrey model, we believe the Gledhill model is slightly more

accurate to this data. We refer to this adjusted model as GPI+. Given that the chemistry in this region of the atmosphere is not well known, we also performed our analysis with three additional models to provide context.

1. The best fit from Vickrey et al. (1982) of multiple observations from several authors of α in the E-region.
$$\alpha(h) = 2.5 \times 10^{-12} e^{-h_{\text{km}}/51.2} \qquad [\text{m}^3 \cdot \text{s}^{-1}]$$
To use this model we needed to extend it into the D-region, where it is not well defined.
2. The observations of Osepian et al. (2009) during a solar proton event on January 17, 2005 at 9:50 UT. While these observations cover the D-region, they must be extended into the E-region. They also only cover a single event and that event is not pulsating aurora.
3. The best fit of Gledhill (1986) for nighttime aurora covering the E-region and D-region.

$$\alpha(h) = 4.3 \times 10^{-6} e^{-2.42\times10^{-2} h_{\text{km}}} + 8.16 \times 10^{12} e^{-0.524 h_{\text{km}}} \qquad [\text{cm}^3 \cdot \text{s}^{-1}]$$

Figure S1 shows how these three additional chemistry model compare with our analysis. They are represented by scatter points around each bar. These points can be considered as rough bounds on our results.

To determine the differential number flux (ϕ) we iterated using the maximum entropy method outlined in Semeter and Kamalabadi (2005). We monitored convergence through the χ^2 value between the modeled ion production rate and the rate calculated from the PFISR measurements. We stopped iterating when the step difference in the χ^2 values was less than 0.01. This usually took between 100 and 1000 steps. From the spectra that converged, we took those with a $1 \leq \chi^2_{\text{reduced}} < 3$ to be suitably good models. To calculate χ^2 it is important to have an accurate description of the variances (errors) in the PFISR data. The data products contain absolute errors associated with the measured number density. To propagate this to the ion production rate we calculated an intermediary recombination coefficient using the simple continuity equation

$$\frac{dn}{dt} = q - \alpha n^2$$

Assuming the temporal change of the electron density, as measured by PFISR, is small compared to the timescales we are studying, we can say that $q = \alpha n^2$, where α is the effective recombination coefficient. From our experience, this steady state assumption is good for pulsating aurora, at least when integrated over 1 minute like the PFISR data is. Previous work has also used it to convert between D-region electron densities and ion production rates (Kirkwood and Osepian, 1995; Osepian et al., 2009). Using this, our errors were then

$$\Delta q_{\text{chem}}(z) = 2\alpha(z) n(z) \Delta n(z)$$

To determine χ^2_{reduced} we need an estimate of the degrees of freedom in the model. We set this as the number of altitude bins where the errors were less than the data (fitted values) minus the number of energy bins (varied values). Figure S2 shows an example fitted electron density using this method. For this visualization, we converted back to electron density from the ion production rates using the same steady state assumption as above.

When performing the inversion, we found that the differential number flux of the highest energy bin was often over an order of magnitude larger than the next highest bin. We believe this is not physical and instead an artifact due to the initial electron density guess only needing to converge to the PFISR sensitivity

($\sim 10^9\ \mathrm{m}^{-3}$) and not zero for lower altitudes. To mitigate this error, we only calculated our averages up to the second highest energy bin.

1.2 PFISR Data

This work uses PFISR data collected in three closely related modes named MSWinds23, MSWinds26, and MSWinds27. All three of these modes interleave three different pulse types optimized for the D-region, E-region, and F-region, respectively, with most of the available duty cycle dedicated to the D-region portion. The D-region portion uses 13-baud Barker codes with $10\ \mu$s baud, oversampled at $5\ \mu$s, with a 2 ms interpulse period (IPP). The E-region portion uses 16-baud randomized alternating code with 30 s baud, and the F-region portion uses $480\ \mu$s uncoded long pulses. Both MSWinds23 and MSWinds26 send 256 consecutive Barker coded pulses in each of the four beam directions and then cycles through the complete set of 32 alternating codes and 32 long pulses on each of the four beam directions. Sending the Barker codes on consecutive pulses allows for the computation of pulse-to-pulse autocorrelation functions and spectra in the D-region, but it has the detrimental effect of introducing range-aliased returns from ranges at integer multiples of 300 km. MSWinds23 transmits the Barker codes and alternating codes on 449.3 MHz and the long pulses on 449.6 MHz. In MSWinds23 the dedicated noise samples on 449.3 MHz are taken by the alternating code channel and need to be rescaled according to the different filter bandwidth to be applied to the Barker code data. MSWinds26 improves this by transmitting the Barker codes on 449.3 MHz, alternating codes on 449.6 MHz, and long pulses on 449.8 MHz, and incorporating dedicated noise samples on all three channels. MSWinds27 is identical to MSWinds26, except it changes the pulse repetition pattern for the Barker codes. Rather than transmitting 256 pulses on each of the four beams, each cycle MSWinds27 transmits 2048 consecutive pulses on the vertical beam and then 128 consecutive pulses on each of the other three beams. This gives MSWinds27 significantly better statistics on the vertical beam at the expense of reduced statistics on the other positions.

This study uses electron density estimated from the received Barker code power and error estimates for that electron density determined from the number of pulses averaged and the signal-to-noise ratio. In addition to random errors, this electron density estimate is potentially subject to systematic bias if the subtracted noise is too small. PFISR has certain hardware issues that cause the noise to be slightly higher at short ranges than at long ranges. Furthermore, the D-region returns can be corrupted by range-aliased F-region returns. Both of these problems bias the lower D-region electron density estimates high. In order to compensate for this bias, we have assumed the true electron density between 55 and 60 km is always indistinguishable from zero. We estimate the bias by averaging the power between 55 and 60 km and subtracting it off from the power profiles before converting to electron density. This bias can be on the order of an electron density of $10^9\ \mathrm{m}^{-3}$, which is a minor correction to the typical electron densities in pulsating aurora (above $10^{10}\ \mathrm{m}^{-3}$). Nonetheless, this bias correction is needed to prevent the inversions from incorrectly estimating tails of relativistic electrons in order to match the lowest altitude data.

REFERENCES

Barrett, J. L. and Hays, P. B. (1976). Spatial distribution of energy deposited in nitrogen by electrons. *Journal of Chemical Physics* 64, 743–750. doi:10.1063/1.432221

Fang, X., Randall, C. E., Lummerzheim, D., Wang, W., Lu, G., Solomon, S. C., et al. (2010). Parameterization of monoenergetic electron impact ionization. *Geophysical Research Letters* 37, L22106. doi:10.1029/2010GL045406

Gledhill, J. A. (1986). The effective recombination coefficient of electrons in the ionosphere between 50 and 150 km. *Radio Science* 21, 399–408. doi:10.1029/RS021i003p00399

Glukhov, V. S., Pasko, V. P., and Inan, U. S. (1992). Relaxation of transient lower ionospheric disturbances caused by lightning-whistler-induced electron precipitation bursts. *Journal of Geophysical Research* 97, 16971–16979. doi:10.1029/92JA01596

Hedin, A. E. (1991). Extension of the MSIS thermosphere model into the middle and lower atmosphere. *Journal of Geophysical Research* 96, 1159–1172. doi:10.1029/90JA02125

Kirkwood, S. and Osepian, A. (1995). Quantitative Studies of Energetic Particle Precipitation Using Incoherent Scatter Radar. *Journal of Geomagnetism and Geoelectricity* 47, 783–799. doi:10.5636/jgg.47.783

Lehtinen, N. G. and Inan, U. S. (2007). Possible persistent ionization caused by giant blue jets. *Geophysical Review Letters* 34, L08804. doi:10.1029/2006GL029051

Marshall, R. A., Xu, W., Kero, A., Kabirzadeh, R., and Sanchez, E. (2019). Atmospheric effects of a relativistic electron beam injected from above: chemistry, electrodynamics, and radio scattering. *Frontiers in Astronomy and Space Sciences* 6, 6. doi:10.3389/fspas.2019.00006

Mitra, A. P. (1981). Chemistry of middle atmospheric ionization - a review. *Journal of Atmospheric and Terrestrial Physics* 43, 737–752. doi:10.1016/0021-9169(81)90050-7

Osepian, A., Kirkwood, S., Dalin, P., and Tereschenko, V. (2009). D-region electron density and effective recombination coefficients during twilight - experimental data and modelling during solar proton events. *Annales Geophysicae* 27, 3713–3724. doi:10.5194/angeo-27-3713-2009

Semeter, J. and Kamalabadi, F. (2005). Determination of primary electron spectra from incoherent scatter radar measurements of the auroral E region. *Radio Science* 40, RS2006. doi:10.1029/2004RS003042

Sivadas, N., Semeter, J., Nishimura, Y., and Kero, A. (2017). Simultaneous Measurements of Substorm-Related Electron Energization in the Ionosphere and the Plasma Sheet. *Journal of Geophysical Research (Space Physics)* 122, 10,528–10,547. doi:10.1002/2017JA023995

Vickrey, J. F., Vondrak, R. R., and Matthews, S. J. (1982). Energy deposition by precipitating particles and Joule dissipation in the auroral ionosphere. *Journal of Geophysical Research* 87, 5184–5196. doi:10.1029/JA087iA07p05184

2 SUPPLEMENTARY TABLES AND FIGURES

2.1 Tables

Table S1.

Filename: pa-pfisr-database-table.xlsx

Caption: Table containing the date, start time, and end time of each pulsating aurora event that we analyzed. These were as seen from the Poker Flat Research Range while the Poker Flat Incoherent Scatter Radar was running during either MSWinds23, MSWinds26, or MSWinds27.

2.2 Figures

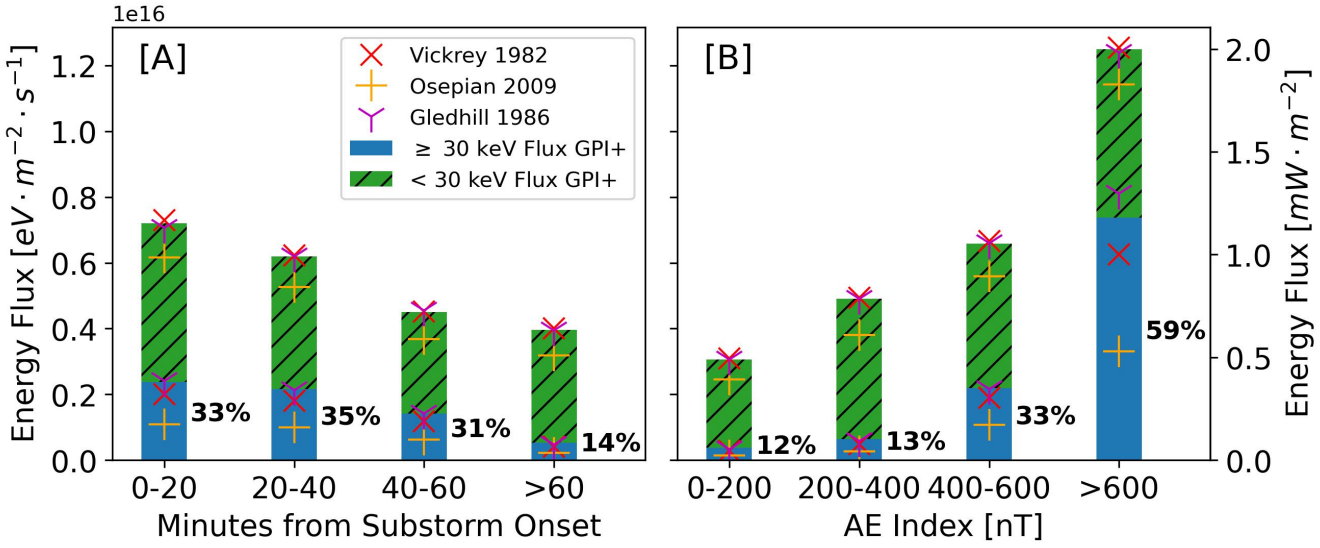

Figure S1. The high ($\geq$ 30 keV) and low ($<$ 30 keV) differential energy flux contributions to pulsating aurora events occurring in four temporal bins relative to substorm onset [A] and AE index [B]. We set the bar heights to the GPI+ model. The scatter points indicate the individual values from the three other chemistry models.

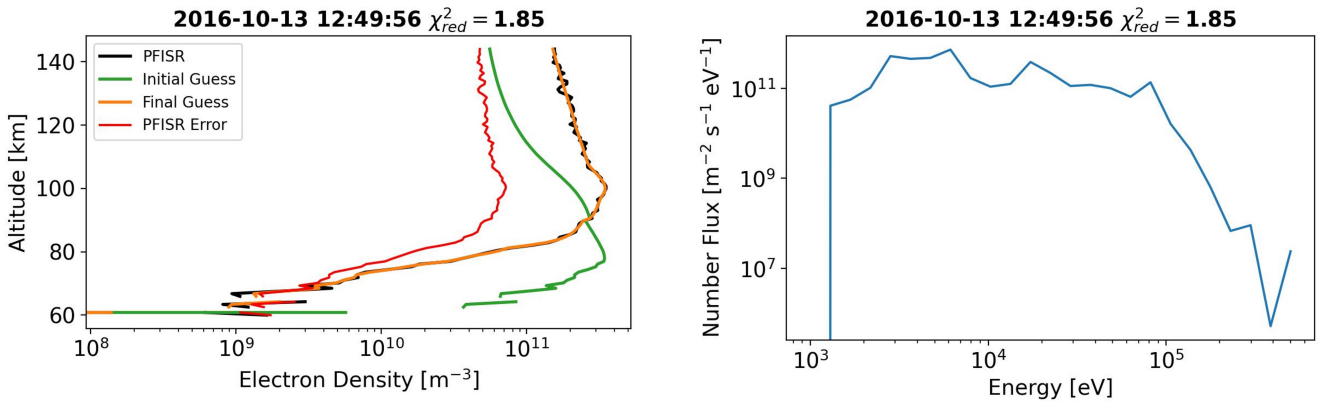

Figure S2. An example fitted electron density using the maximum entropy method along with the GPI+ chemistry model. The plot on the left shows the PFISR measured electron density (black) along with the associated error (red). The initial guess is shown in green and the final fit is shown in orange. The plot on the right is the differential number flux over the range of energies given to the model.

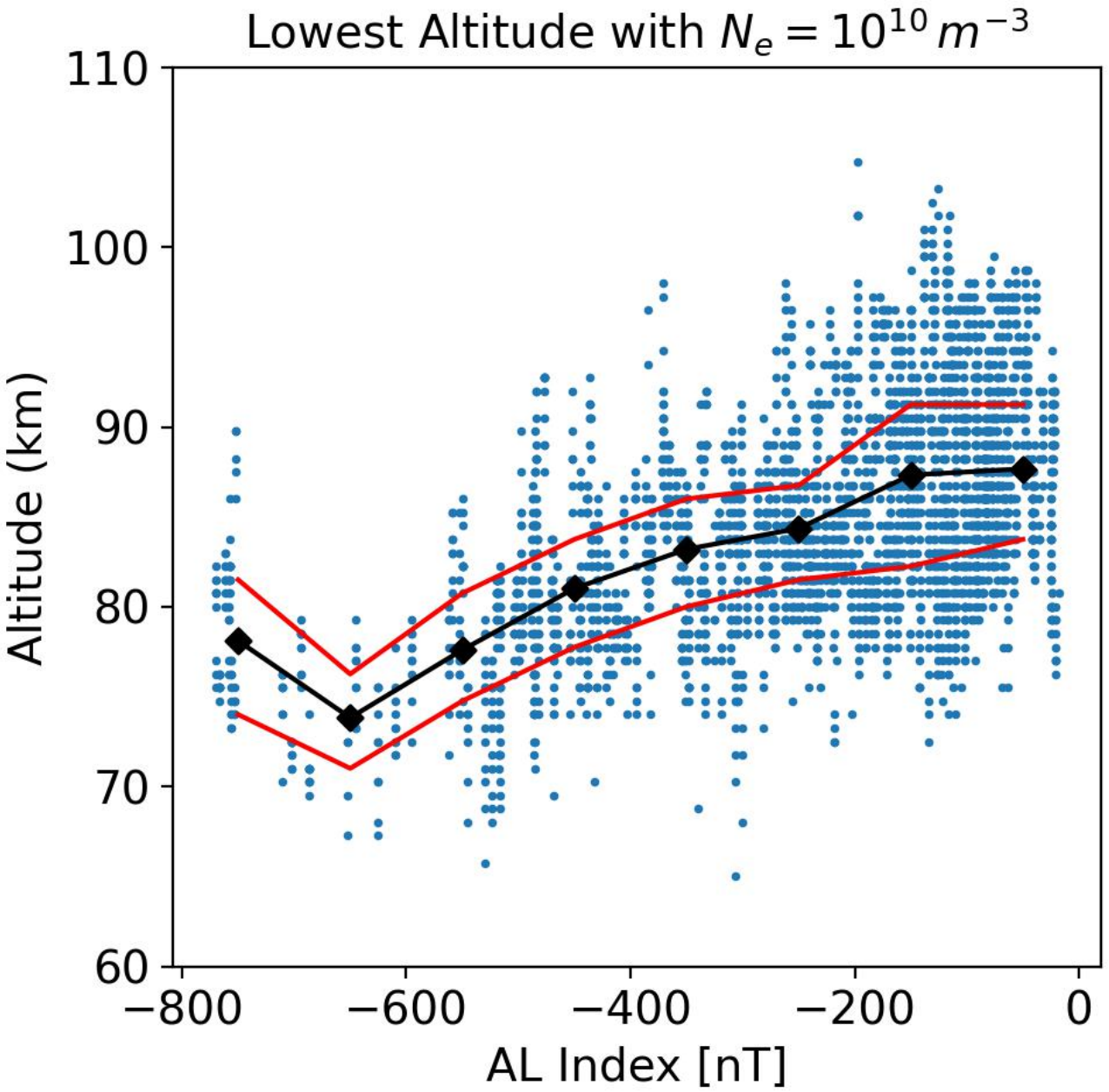

Figure S3. Lowest altitude PFISR measurements during pulsating aurora with $N_e = 10^{10}\,\mathrm{m}^{-3}$ plotted versus AL indices. The black diamonds indicate the average altitude for the surrounding 200 nT. The red lines indicate the 25% and 75% quartiles..

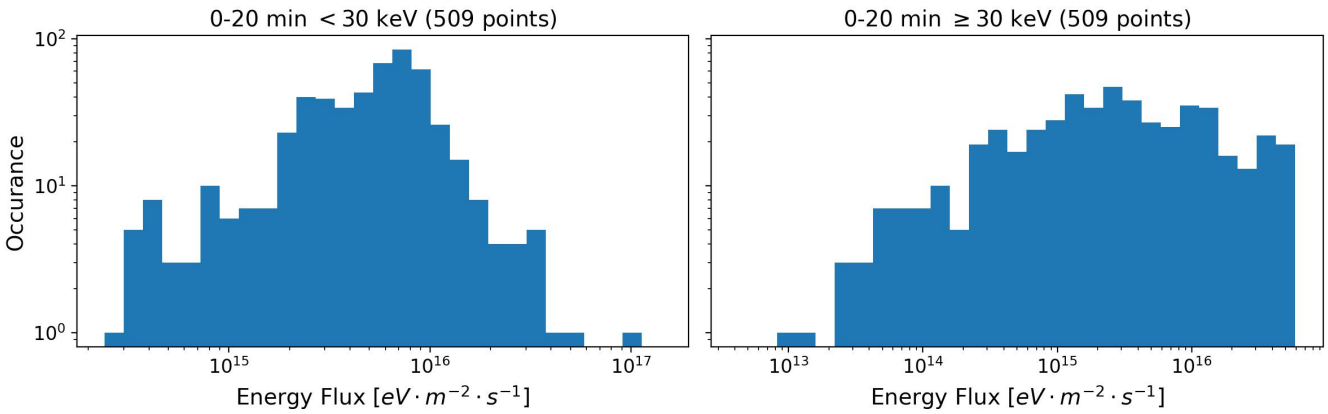

Figure S4. Histogram of total energy flux for the 0-20 minute bin.

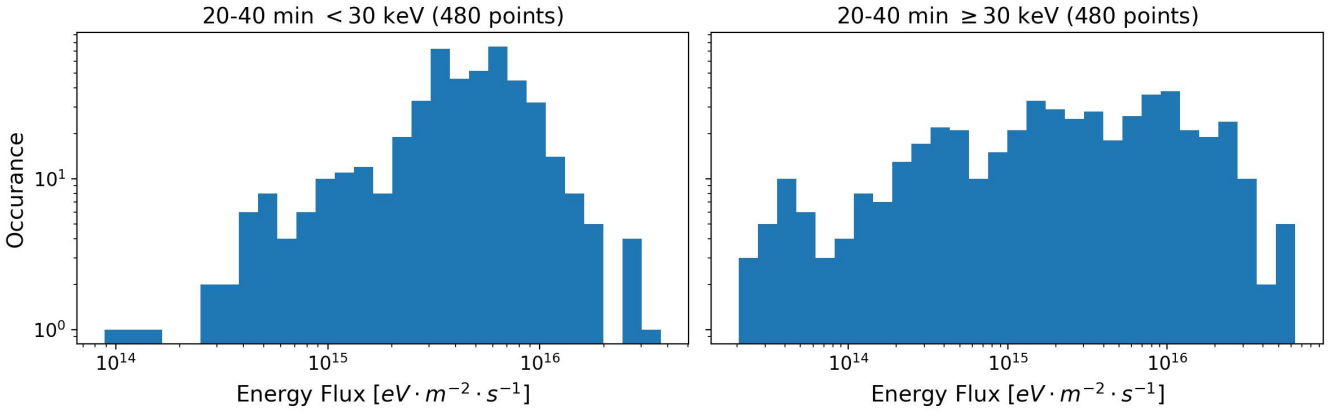

Figure S5. Histogram of total energy flux for the 20-40 minute bin.

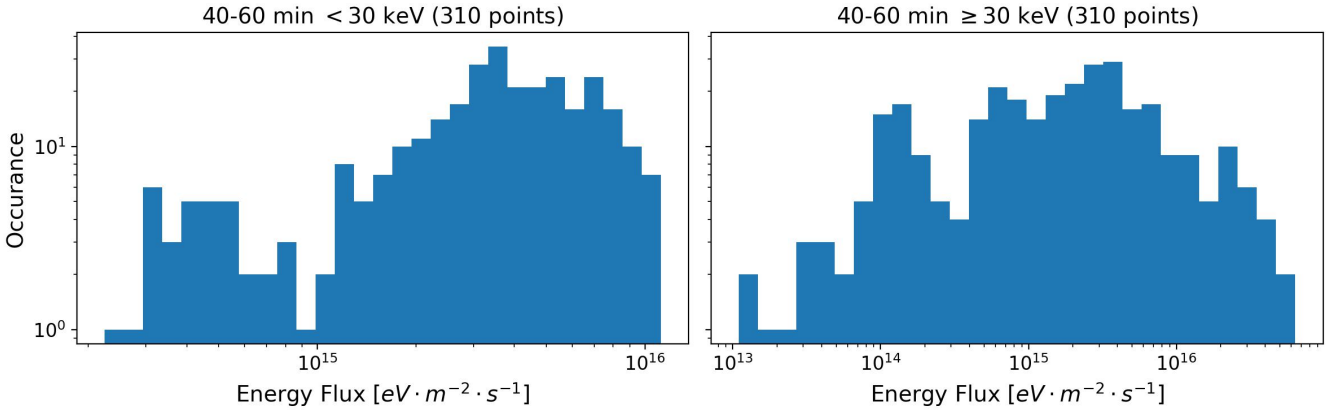

Figure S6. Histogram of total energy flux for the 40-60 minute bin.

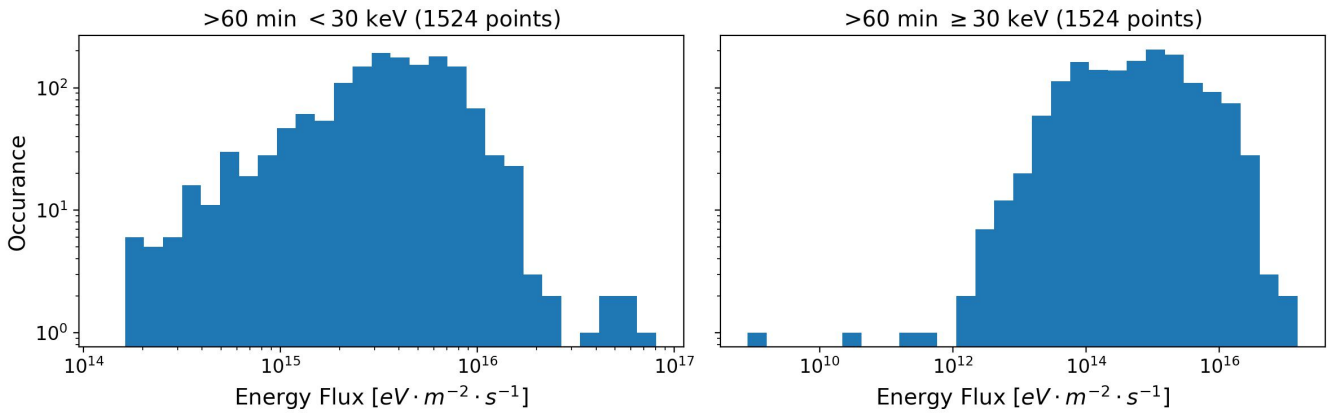

Figure S7. Histogram of total energy flux for the > 60 minute bin.